High Power Laser Science and Engineering, (2020), Vol. 8, e1, 6 pages.
doi:10.1017/hpl.2020.2

HIGH POWER LASER SCIENCE AND ENGINEERING

RESEARCH ARTICLE

High-efficiency 50 W burst-mode hundred picosecond green laser

Ning Ma, Meng Chen, Ce Yang, Shang Lu, Xie Zhang, and Xinbiao Du

Institute of Laser Engineering, Beijing University of Technology, Beijing 100124, China

(Received 23 October 2019; revised 9 December 2019; accepted 7 January 2020)

Abstract

We report high-energy, high-efficiency second harmonic generation in a near-infrared all-solid-state burst-mode picosecond laser at a repetition rate of 1 kHz with four pulses per burst using a type-I noncritical phase-matching lithium triborate crystal. The pulses in each burst have the same time delay (∼1 ns), the same pulse duration (∼100 ps) and different relative amplitudes that can be adjusted separately. A mode-locked beam from a semiconductor saturable absorber mirror is pulse-stretched, split into seed pulses and injected into a Nd:YAG regenerative amplifier. After the beam is reshaped by aspheric lenses, a two-stage master oscillator power amplifier and 4f imaging systems are applied to obtain a high power of ∼100 W. The 532 nm green laser has a maximum conversion efficiency of 68%, an average power of up to 50 W and a beam quality factor M^2 of 3.5.

Keywords: all-solid-state laser; high-power laser; second harmonic generation

1. Introduction

Burst-mode picosecond green lasers with a high pulse energy and high average power have important applications in many fields. One of the most promising applications is space debris laser ranging. Monitoring and early warning of space debris have attracted considerable attention worldwide owing to a dramatic increase in space garbage, which poses a serious threat to spacecraft operation and human space activities. Moreover, space debris laser ranging technology not only enables real-time space debris orbit measurement with high precision (one or two orders of magnitude higher than that of other ground-based observation equipment) but also provides calibration for other monitoring methods. Nanosecond lasers are currently used as the light source for space debris laser ranging because they are readily available at higher pulse energies than picosecond lasers. However, the use of lasers with picosecond pulses can afford improved ranging precision owing to their narrow pulse duration; in addition, their pulses are longer than femtosecond pulses, enabling the detector to respond. Because the laser beam is diffusely reflected by space debris, however, a higher laser pulse energy is needed for the detector to capture the reflected photons. As the pulse energy increases, smaller and more distant space debris can be measured, and raising the repetition rate of the laser shortens the time interval between adjacent diffusely reflected pulses, improving the speed of target acquisition. A recent study showed that using a double-pulse picosecond laser for tracking space debris increases the ranging precision of laser space debris measurement from the decimeter level to the centimeter level. Besides, burst-mode lasers also have advantages in the fields of fine machining application and scientific research.

Various methods have been proposed to obtain high-pulse-energy and high-average-power ultrashort green lasers for high-energy ultrafast laser systems; these include beam shaping techniques, chirped-pulse amplification (CPA), beam combining and nonlinear interactions, which can all maximize the pulse energy extraction and reduce the damage threshold requirement of subsequent optical components. In 2013, Noom *et al.* reported a laser amplification system with a top-hat intensity profile that produces 130 mJ, 64 ps pulses at 1064 nm; after frequency doubling, 75 mJ, 64 ps pulses were obtained at 532 nm with a repetition rate of 300 Hz and a conversion efficiency of 50%. However, the beam shaping efficiency was less than 1% (a pulse energy output of only 0.07 mJ for a 1.2 mJ input). In 2016, Adamonis *et al.* used a spatially variable wave plate for beam shaping, which reshaped the seed beam into a 12th-order super-

Correspondence to: M. Chen, Institute of Laser Engineering, Beijing University of Technology, Beijing 100124, China.
Email: picolaser_chen@163.com

Gaussian beam with an efficiency of approximately 50%; the output beam power in both channels was 130 W at 1064 nm. Further, using noncollinear frequency up-conversion in a lithium triborate (LBO) crystal, they obtained 150 mJ, 85 ps green light at a repetition rate of 1 kHz. The conversion efficiency was approximately 58%.

CPA technology is used mainly in femtosecond laser systems, where a broader linewidth in the gain medium is useful. Pulse duration broadening to the picosecond level is also a somewhat effective way to avoid optical damage and obtain a high average power without increasing the number of optical components, although the spectral linewidth of picosecond pulses, which is narrower than that of femtosecond pulses, limits their broadening efficiency. In 2017, Long *et al.* reported that a laser pulse duration of 23.5 ps was broadened to 115 ps by a volume Bragg grating (VBG), and, after two-stage Nd:YAG traveling-wave amplification, the laser exhibited an average power of 96 W at 1064 nm.

Beam combining, including coherent beam combining and spectral beam combining, is another way to obtain high-power lasers. To realize a high peak power using fiber amplifiers, in 2017, Želudevičius *et al.* obtained an overall conversion efficiency of 51% and an average power of 29 W at 532 nm with a pulse duration of ∼200 ps using pulse multiplexing and beam combining of four pulsed Yb-doped fiber lasers by noncollinear frequency up-conversion in an LBO crystal.

In this study, we designed a high-pulse-energy, high-average-power burst-mode picosecond laser system for space debris laser ranging. It consists of a semiconductor saturable absorber mirror (SESAM) mode-locked picosecond oscillator, VBG pulse stretcher, pulse splitting system designed to obtain a nanosecond pulse interval in the burst, a burst-mode regenerative amplifier (RA) and a ring pattern beam reshaping system consisting of two aspheric lenses, two-stage power amplifiers and a high-efficiency frequency doubler. Moreover, it adopts the collinear output of the fundamental beam and second harmonic generation (SHG), and both frequency pulses can be used simultaneously for space debris laser ranging to improve the measurement accuracy or operated independently. In particular, the fundamental beam, which can operate during the day, reduces the effect of the sun. Further, the relative amplitude of each pulse in the burst, as well as the pulse interval, can be easily adjusted, which is convenient for experimental research on space debris ranging. The aspheric lens system reshapes the Gaussian beam output by the RA to a ring profile with high conversion efficiency, which reduces the difficulty of subsequent amplification; consequently, an average power of up to 50 W at 532 nm is obtained, which corresponds to a pulse envelope energy of 50 mJ, and the second harmonic conversion efficiency reaches 68%.

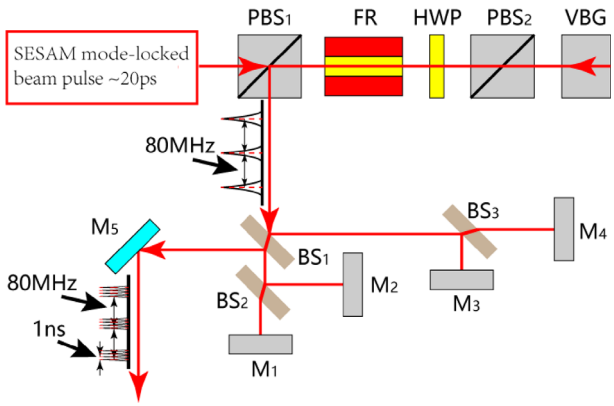

Figure 1. Schematic diagram of the seed laser. PBS_1, PBS_2: polarization beam splitters; FR: Faraday rotator isolator; HWP: half-wave plate; VBG: volume Bragg grating; BS_1–BS_3: beam splitters; M_1–M_5: high-reflectivity mirrors.

2. Experimental setup

The seed laser, which is shown schematically in Figure 1, consists of a home-built Nd:YVO_4 SESAM mode-locked laser with a repetition rate of 80 MHz and a pulse duration of ∼20 ps, a Faraday isolator that protects the oscillator from potential feedback from subsequent components, a pulse stretcher and a burst-mode setup. In the single-pass pulse stretcher, a VBG with a modulation coefficient of 550 ps/nm is used. After the beam travels through the VBG (4 mm × 4 mm × 18 mm), the pulse duration of the seed laser is broadened to ∼100 ps, and the power decreases to 878 mW, which corresponds to a diffraction efficiency of 80%. Four pulses per burst are obtained using an improved Michelson interferometer. BS1, BS2 and BS3 are beam splitters with 50:50 beam splitting at a 45° incidence angle. By choosing appropriate length intervals between mirrors M2–M5, which gradually increase by equal increments (ΔL), we can obtain pulses in bursts with equal time delays of Δt. To meet the requirements for space debris measurement and accommodate the high-voltage operation time of a Pockels cell (PC; which operates as a pulse selection switch) in the RA, a time delay of ∼1 ns ($\Delta t = 2 \times \Delta L/c$, where c is the speed of light) is obtained by setting $\Delta L = 150$ mm.

To realize high-power, high-energy picosecond pulsed lasers, a diode-side-pumped Nd:YAG RA and a two-stage traveling-wave amplification are adopted for the amplifier system, as shown in Figure 2. The Nd:YAG RA, which acts as a pre-amplifier, reduces the repetition rate of the seed laser from 80 MHz to 1 kHz by electro-optic modulation. The seed laser is injected into the RA through the optical isolation system from P_1 and then output from P_1 after amplification. And the FR and HWP1 act as an optical isolation system to avoid the influence of the output amplified beam returning to the seed oscillation cavity on the seed optical stability. The quarter-wave plate (QWP) and PC constitute the pulse

https://doi.org/10.1017/hpl.2020.2 Published online by Cambridge University Press

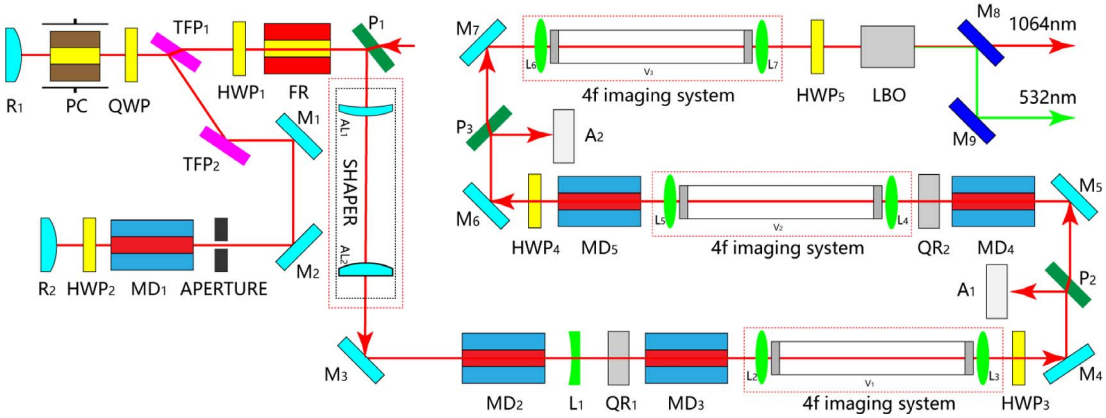

Figure 2. Schematic diagram of the amplifier and SHG construction. P_1–P_3: polarizers; FR: Faraday rotator isolator; HWP_1–HWP_5: half-wave plates; TFP_1, TFP_2: thin-film polarizers; QWP: quarter-wave plate; PC: Pockels cell; R_1, R_2: convex mirrors; M_1–M_7: high-reflectivity mirrors; MD_1–MD_5: Nd:YAG modules; AL_1, AL_2: aspheric lenses; L_1–L_7: lenses; V_1–V_3: vacuum tubes; QR_1, QR_2: 90° quartz rotators; A_1, A_2: aluminum blocks; M_8, M_9: dichroic mirrors.

selected switch in the RA. The pumping module (MD_1) has a central wavelength of 808 nm with a repetition rate of 1 kHz. The dimension of the Nd:YAG crystal rod is Φ 4 mm × 67 mm with 1 at.% doped. Then, the Gaussian output beam of the RA is converted into a ring-shaped beam using an aspheric lens reshaping system with a conversion efficiency of approximately 93%. The total length of the shaping system we used is 90 mm, which is a typical Galilean configuration (without internal focusing), consisting of two aspheric lenses. The front surface of the first lens is concave to ensure that no rays cross the optical axis and the back surface is aspheric; the second lens has an aspheric–planar structure. The apertures of two aspheric lenses are 8 mm and 15 mm, respectively, and both sides of the lenses are coated with an anti-reflection film of 1064 nm. The purpose of shaping is to reduce the central light intensity of the spot and avoid self-focusing during amplification. To maintain the beam quality during the two-stage single-pass double-module amplification, two 4f imaging systems are used, and all the subsequent imaging systems contain vacuum tubes to prevent air breakdown. The laser-diode-pumped bars of two modules in each stage are arranged at complementary angles to reduce the depolarization loss. The same as MD_1, all of the pumping modules used in the power amplifiers have a central wavelength of 808 nm with a repetition rate of 1 kHz. Two modules in each stage are powered by the same power supply and cooled by the same waterway, and the cooling water temperature is set to 25°. The dimension of the Nd:YAG crystal rods used in the first-stage pumping modules is Φ 4 mm × 67 mm with 1 at.% doped. In the second-stage modules, the dimension of the crystal rods is Φ 6 mm × 85 mm with 0.8 at.% doped. A half-wave plate and 90° quartz rotator help to compensate for the difference in optical power between the tangential and radial polarization components of the thermal lens. To improve the degree of polarization, two 45° polarizers are used to remove

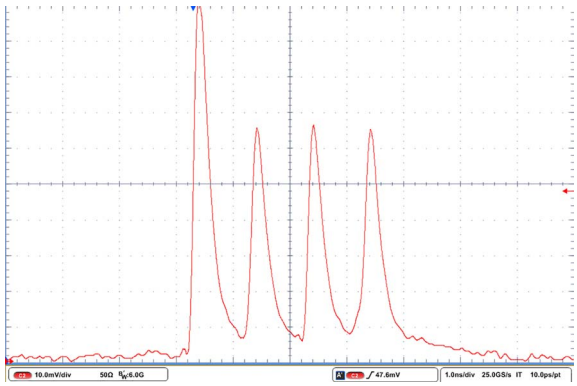

Figure 3. Waveform of RA.

the vertically polarized light added during amplification. L_1 is a plane concave lens used to compensate for the thermal lens, and all of the amplifier modules are synchronized between the seed and pump pulses with a pump pulse width of 200 μs.

The frequency conversion module, which is used to adjust the beam size and divergence, is placed behind the 4f imaging system to realize the highest conversion efficiency. To further improve the conversion efficiency, a thin-film polarizer at 1064 nm is used to purify the polarization direction of the amplified fundamental light. The second harmonic waves are generated by an LBO crystal (6 mm × 6 mm × 15 mm), which was chosen for its excellent performance: a high damage threshold, relatively high nonlinearity, a large acceptance angle and no spatial walk-off for type-I noncritical phase matching at 1064 nm. The crystal is combined with a half-wave plate to obtain the best phase-matching condition. The LBO crystal is placed in an oven at 149 °C with a control accuracy of ±0.05 °C. To measure the efficiency of light frequency doubling, two dichroic mirrors

https://doi.org/10.1017/hpl.2020.2 Published online by Cambridge University Press

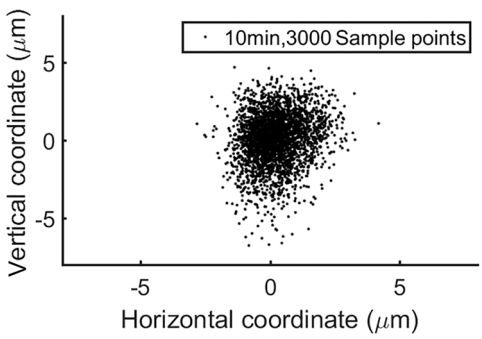

Figure 4. Beam direction fluctuation.

with 45° incidence are employed to separate the fundamental wave at 1064 nm and the second harmonic wave at 532 nm.

3. Experimental results

Owing to the properties of the RA, the coupling efficiency between the injected beam field and the regenerative cavity affects only the output beam intensity, not the beam direction; therefore, we can adjust the relative amplitude of each pulse in the bursts without affecting the collinearity of each sub-pulse by fine-tuning the mirrors behind the splitters, which changes the coupling efficiency of each sub-pulse injected into the regenerative cavity. In the waveform in Figure 3, the first pulse in the burst has a higher amplitude than the following three pulses, which have equal amplitudes. Note that we can also produce multiple pulses within each burst with the equivalent amplitude to satisfy different applications. When the average pump power is set to 105 W at 808 nm, the average output power reaches 9 W after 25 extraction cycles in the regenerative amplifying cavity, and the beam diameter is ∼1.5 mm. Figure 4 shows the fluctuation of the direction of the beam output from the RA, which is less than ±25 μrad, as measured by a convex lens with a focal length of 200 mm and a camera with pixel dimensions of 5.5 μm × 5.5 μm. The beam from the RA is Gaussian, and its shape is optimized by a Galilean beam expander system composed of two aspheric lenses. The first lens redistributes the intensity of the Gaussian beam, and the second lens collimates the beam. After passing through the shaping system, the beam has a ring-shaped profile without a strong central intensity distribution, as shown in Figure 5. After the first-stage amplifier (the total average pump power of two side-pump Nd:YAG modules is 605 W at 808 nm), the 8.4 W power is amplified to 31.4 W. Through HWP_3 and P_2, the power reduces to 28.9 W, corresponding to the depolarization rate of 8.0%. Through the second-stage amplifier, the depolarization rate is 7.8%. The lower depolarization rate of the second-stage amplifier is due to the use of an array of five symmetrical laser-diode-pumped bars as pumping modules, which makes the thermal load distribution in the Nd:YAG rod more uniform, while the modules (MD_2, MD_3) used in the first-stage amplifier are three symmetrical laser-diode-pumped bars. After the amplifier system (the total average pump power of MD_4 and MD_5 increases to 1036 W at 808 nm), an average power of more than 80 W with a 0.56% power fluctuation over 30 min (Figure 6) is obtained at a repetition rate of 1 kHz, and the beam diameter is ∼5.5 mm.

Figure 7 shows the spectral evolution of the system from narrowing to broadening. Specifically, the dominant peak of the spectrum after the RA narrows from 0.187 to 0.112 nm and is slightly red-shifted. The main reason for the central wavelength shift is the use of two different gain media. The gain medium in seed laser cavity is Nd:YVO_4, while the gain medium used in the RA is Nd:YAG. However, the subsequent traveling-wave amplification causes spectral broadening with a two-peak structure. The physical mechanism of the spectral red shift and distortion is the self-phase modulation caused by gain saturation.

Frequency doubling is performed by controlling the fundamental beam with a small divergence angle into a 15-mm-long LBO at 90° incidence. The size of the fundamental beam is no less than 5 mm, and the pulse peak intensity is as high as 2 GW/cm^2 but less than the damage threshold of the LBO. Figure 8 plots the dependence of the green power

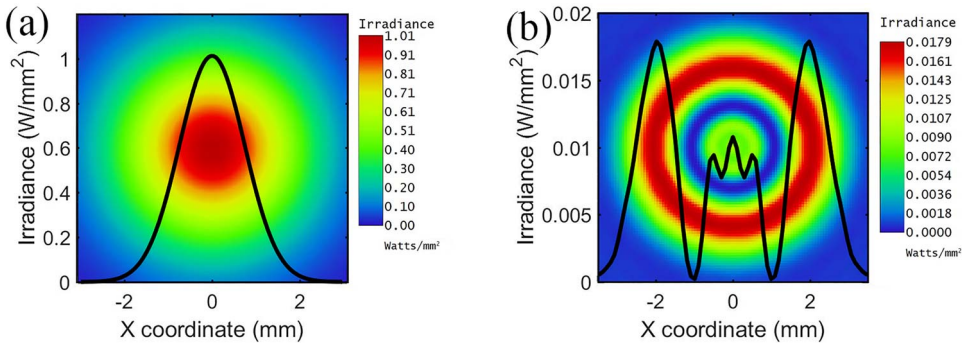

Figure 5. Intensity distributions of (a) input Gaussian beam (TEM_{00} laser) and (b) laser after the shaping lens.

https://doi.org/10.1017/hpl.2020.2 Published online by Cambridge University Press

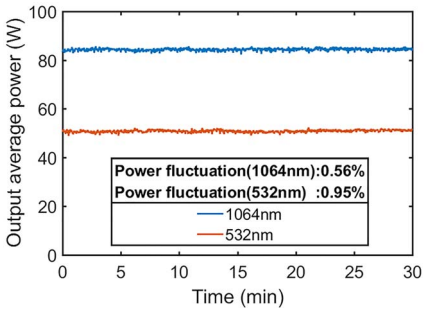

Figure 6. Power fluctuation at 1064 and 532 nm.

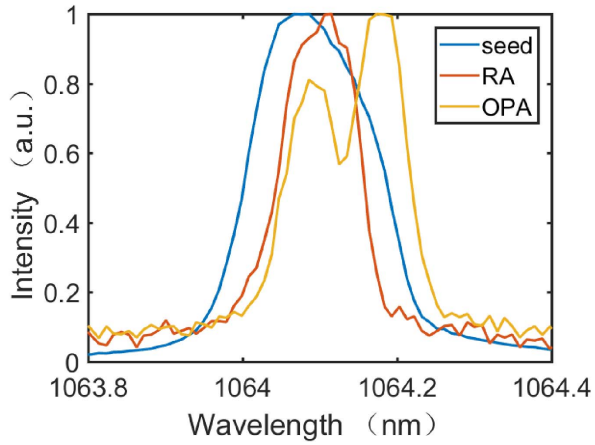

Figure 7. Spectral evolution of the system. The spectral widths of the seed, RA and oscillator power amplifier are 0.187, 0.112 and 0.142 nm, respectively.

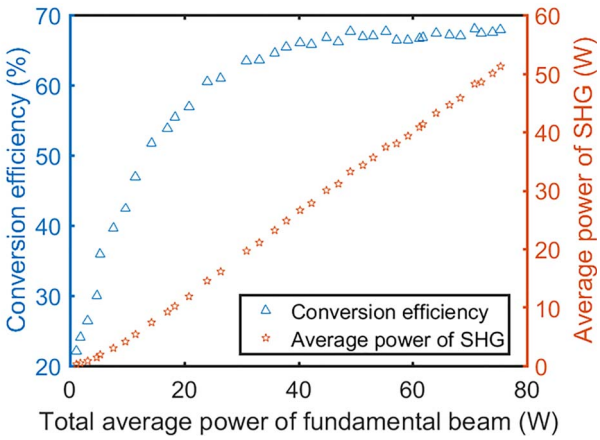

Figure 8. Dependence of the green power and second harmonic conversion efficiency on the incident fundamental power.

and second harmonic conversion efficiency on the incident fundamental power. The conversion efficiency increases monotonously with increasing incident power and reaches a maximum value of 68% at 40 W. Then, it fluctuates around 66% by 2%. By increasing the infrared power, we obtained green light with a power of up to 50 W and a

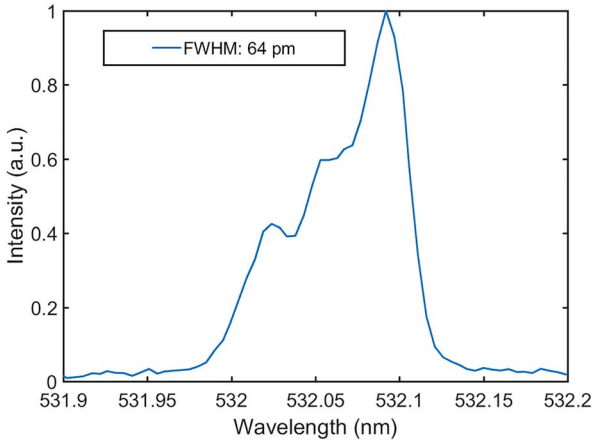

Figure 9. Spectrum of the SHG.

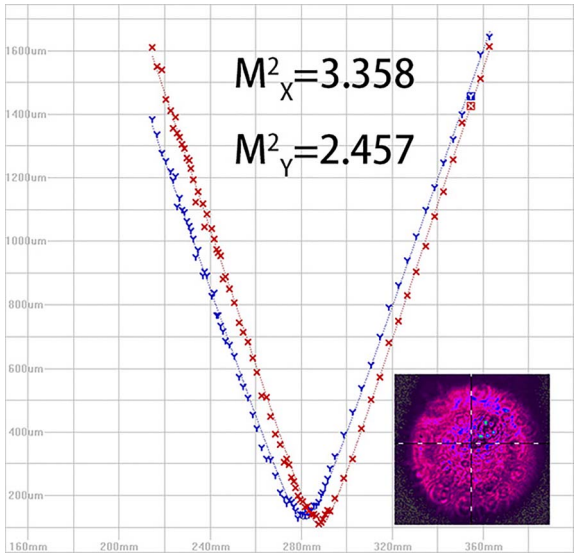

Figure 10. Beam quality of SHG.

power fluctuation of less than 1%, as shown in Figure 6. Similar to that of the amplified pulse, the spectrum of the green light has an asymmetric shape with a full-width at half-maximum of 64 pm, as shown in Figure 9. Figure 10 shows that the intensity distribution profile and beam quality factors of the green laser were $M_x^2 = 3.358$ in the x direction and $M_y^2 = 2.457$ in the y direction at the output fundamental power of ~80 W.

4. Conclusion

In conclusion, we experimentally demonstrated a burst-mode picosecond laser system with a high pulse energy, high average power and high frequency doubling efficiency for space debris laser ranging. In this system, pulse stretching, beam splitting and reshaping by aspheric lenses are used

https://doi.org/10.1017/hpl.2020.2 Published online by Cambridge University Press

to realize high-power laser output. After two-stage master traveling-wave amplification, the power of the fundamental beam is as high as 80 W with a power fluctuation of 0.56% over 30 min. By properly passing the beam through a type-I noncritical phase-matching LBO crystal, a 50 W second harmonic laser with less than 1% power fluctuation over 30 min is obtained at a pulse repetition rate of 1 kHz with a conversion efficiency of 68%. The laser system, which emits co-channel burst-mode pulses with a narrow linewidth and high intensity at 1064 and 532 nm, provides a promising light source for high-precision laser ranging of small space debris.

Acknowledgement

This research was supported by the National Natural Science Foundation of China (No. U1631240).

References

1. G. Kirchner, F. Koidl, F. Friederich, I. Buske, U. Völker, and W. Riede, Adv. Space Res. **51**, 21 (2013).
2. Z. Zhang, H. Zhang, M. Long, H. Deng, Z. Wu, and W. Meng, Optik **179**, 691 (2019).
3. C. Kerse, H. Kalaycioglu, P. Elahi, B. Cetin, D. K. Kesim, O. Akcaalan, S. Yavas, M. D. Asik, B. Oktem, H. Hoogland, R. Holzwarth, and F. O. Ilday, Nature **537**, 84 (2016).
4. X. Q. Gao, M. L. Long, and C. Meng, Appl. Opt. **55**, 6554 (2016).
5. J. A. Hoffnagle and C. M. Jefferson, Appl. Opt. **39**, 5488 (2000).
6. M. L. Long, L. Y. Chen, M. Chen, and G. Li, Appl. Phys. B **122**, 142 (2016).
7. J. Želudevičius, K. Regelskis, and G. Račiukaitis, Opt. Lett. **42**, 175 (2017).
8. H. Yuan, Y. Wang, Q. Yuan, D. Hu, C. Cui, Z. Liu, S. Li, Y. Chen, F. Jing, and Z. Lu, High Power Laser Sci. Eng. **7**, e41 (2019).
9. D. W. E. Noom, S. Witte, J. Morgenweg, R. K. Altmann, and K. S. E. Eikema, Opt. Lett. **38**, 3021 (2013).
10. J. Adamonis, A. Aleknavicius, K. Michailovas, S. Balickas, V. Petrauskiene, T. Gertus, and A. Michailovas, Appl. Opt. **55**, 8007 (2016).
11. Z. H. Wang, C. Liu, Z. W. Shen, Q. Zhang, H. Teng, and Z. Y. Wei, Opt. Lett. **36**, 3194 (2011).
12. D. Strickland and G. Mourou, Opt. Commun. **56**, 219 (1985).
13. M. L. Long, G. Li, and M. Chen, Appl. Opt. **56**, 4274 (2017).
14. J. E. Murray and W. H. Lowdermilk, J. Appl. Phys. **51**, 3548 (1980).
15. M. Grishin, V. Gulbinas, and A. Michailovas, Opt. Express **15**, 9434 (2007).
16. A. Penzkofer and N. Weinhardt, IEEE J. Quantum Electron. **19**, 567 (1983).
17. G. P. Agrawal and N. A. Olsson, IEEE J. Quantum Electron. **25**, 2297 (1989).

https://doi.org/10.1017/hpl.2020.2 Published online by Cambridge University Press